sPHENIX | Note

tag: sPH-CONF-JET-2025-02
version: 1
DOI: unspecified
date: April 3, 2025

sPHENIX Conference Note

Measurement of isolated prompt photons in $p+p$ collisions at $\sqrt{s} = 200$ GeV with the sPHENIX detector

sPHENIX Collaboration

Abstract

This sPHENIX Conference Note reports the measurement of the isolated prompt photon cross-section as a function of transverse energy (E_{T}^{γ}) in proton–proton collisions at $\sqrt{s}$ = 200 GeV, using data collected in 2024 with the sPHENIX detector at the Relativistic Heavy Ion Collider with integrated luminosity of 16.6 pb^{-1}. Photons are measured within $|\eta^{\gamma}| <$ 0.7 and $10 < E_{\mathrm{T}}^{\gamma} < 26$ GeV. They are reconstructed using the Electromagnetic Calorimeter and identified using electromagnetic shower shapes. An isolation selection using both the Electromagnetic and Hadronic Calorimeters is applied to suppress both fragmentation photons and background photons mostly originating from neutral-meson decays. The E_{T}^{γ} yield is corrected for purity and efficiency, and then unfolded for detector response. The E_{T}^{γ}-differential cross-sections are compared with theoretical predictions from Monte Carlo generator PYTHIA-8 as well as next-to-leading-order perturbative Quantum Chromodynamics calculations including JETPHOX.

1 Introduction

Prompt photons refer to those produced either directly from parton-parton scattering, so-called *direct photons*, or from the collinear fragmentation of a final-state parton, so-called *fragmentation photons*. At leading order (LO), direct photons are produced predominantly from quark–gluon Compton scattering and quark–antiquark annihilation processes. At next-to-leading-order (NLO), additional contributions come from final-state fragmentation and radiation into photons.

The production of prompt photons can be calculated within the framework of perturbative Quantum Chromodynamics (pQCD); therefore, prompt photons provide a stringent test of pQCD predictions. Furthermore, prompt photon production is particularly sensitive to the gluon parton distribution function (PDF) in the proton when the quark–gluon Compton process is dominant, providing insight into gluon dynamics in hadronic collisions.

To reduce the contribution of fragmentation photons and background photons from hadron decays, an isolation requirement can be imposed. This involves restricting the amount of transverse energy surrounding the photon within a fixed cone in pseudorapidity (η) – azimuthal angle (ϕ) space.

Isolated prompt photon cross-sections have been extensively measured at the Large Hadron Collider (LHC) in p+p collisions [1, 2, 3, 4, 5, 6] as well as in p+Pb [7, 8] and Pb+Pb [9, 10, 11] collisions across various collision energies. At the Relativistic Heavy-Ion Collider (RHIC) [12], the PHENIX experiment reported prompt photon cross-sections without an isolation requirement [13]. These p+p measurements provide a crucial baseline for identifying possible modifications of the initial parton distributions in the nuclear medium by comparing photon-tagged jet events in heavy-ion collisions against the p+p reference.

In this note, the E_{T}^{γ}-dependent cross-section of isolated prompt photons in p+p collisions at $\sqrt{s}$ = 200 GeV is presented, using a subset of the 2024 data corresponding to an integrated luminosity of 16.6 pb^{-1}, which is approximately 15% of the total collected data. We define photons to be isolated if the total transverse energy of final-state particles within $\Delta R = 0.3$ of the photon is less than 4 GeV. The results are compared to NLO pQCD calculations from JETPHOX [14], L.E. Gordon and W. Vogelsang [15] as well as the Monte Carlo (MC) generator PYTHIA-8 [16]. The sPHENIX results are also compared to direct photon measurements reported by the PHENIX experiment.

2 sPHENIX detector

sPHENIX [17, 18] is a new detector designed to measure jet and heavy-flavor probes of the quark-gluon plasma (QGP) created in Au+Au collisions at the RHIC. A precision tracking system enables measurements of heavy-flavor and jet-substructure observables while the electromagnetic and hadronic calorimeter system is crucial for measuring the energy of jets and identifying direct photons and electrons.

Going outwards starting from the beam line, sPHENIX comprises the following subsystems [19]: the MAPS-based Vertex Detector (MVTX); the INTermediate Tracker (INTT); the Time Projection Chamber (TPC) [20]; the Time Projection Chamber Outer Tracker (TPOT) [21]; the Electromagnetic Calorimeter (EMCAL) [22, 23]; the Inner Hadronic Calorimeter (IHCAL) [23]; the 1.4 T superconducting solenoid magnet [24] and the Outer Hadronic Calorimeter (OHCAL) [23]. Except for TPOT, all detectors have full azimuthal coverage and span $|\eta| < 1.1$ in pseudorapidity. sPHENIX also includes a number of forward detectors, namely the Minimum Bias Detectors (MBD), the sPHENIX Event Plane Detectors (sEPD), and the Zero Degree Calorimeters (ZDC), that includes the Shower Maximum Detector (SMD).

sPHENIX began its commissioning process in RHIC Run-2023 with Au+Au collisions at $\sqrt{s_{_{NN}}}$ = 200 GeV. During RHIC Run-2024, sPHENIX collected a large sample of transversely polarized p+p physics data at $\sqrt{s}$=200 GeV, alongside a smaller sample of Au+Au data to complete its commissioning phase in that collision system.

3 Analysis Procedure

3.1 Event Selection

Events were recorded using a combination of photon and minimum-bias triggers. The minimum-bias trigger requires a coincident charge signal in at least one photomultiplier tube on both sides of the MBD, consistent with the energy deposit of a minimum ionizing particle. The photon trigger requires an EMCAL energy threshold of 4 GeV in an 8×8 tower region (each tower covers a 0.025×0.025 segment in η–ϕ). Events are required to have a reconstructed MBD z-vertex in the range of $|z_{\mathrm{vertex}}| < 30$ cm.

3.2 Monte Carlo Simulations

Simulated prompt photon events are generated with PYTHIA-8.307 [16] with the Detroit tune [25]. Direct and fragmentation photons are generated and used for efficiency corrections, unfolding and the purity signal-leakage correction. Inclusive jet samples, including photons decayed from neutral mesons, are used to optimize the photon identification (γ^{ID}) and sideband requirements. The generated PYTHIA-8 events are then propagated through the full sPHENIX detector using the GEANT-4 simulation package [26] with noise effect added to match the data. Photons are reconstructed the same way as the data. To account for systematic differences arising from the mis-modeling of isolation energy in the simulation, corrections are applied to the simulated isolation transverse energy ($E_{\mathrm{T}}^{\mathrm{iso}}$) to better match the data.

At the truth level, signal photons are defined as prompt photons (including both direct and fragmentation photons) that satisfy the isolation requirement: the total transverse energy of all final state particles within $\Delta R = 0.3$, excluding neutrinos and the photon itself, is below 4 GeV. Reconstructed photons are considered to be matched to truth signal photons if they are within $\Delta R < 0.05$.

3.3 Photon Reconstruction and Identification

Photon candidates are reconstructed by clustering EMCAL towers. Superclusters are formed by grouping contiguous towers with energies above 70 MeV, which is around 2 to 3 standard deviations of the pedestal RMS. Additionally, a supercluster is required to have a total energy exceeding 0.5 GeV and contain at least one tower with energy above 0.2 GeV. Superclusters are then divided into sub-clusters using a local peak-finding algorithm within a 3×3 tower grid [27]. Reconstructed photons have a resolution of approximately 6% across the entire E_{T}^{γ} range.

Photon candidates are identified by leveraging the differences between electromagnetic shower shapes among electromagnetic probes, i.e., photons and electrons, and hadrons. One of the shower-shape variables with the greatest separation power between signal and background is w_{η}, defined as the second moment of the EMCAL tower η distribution, weighted by the energies of the towers in a cluster. Another variable, E_{t1}, is defined as the sum of the tower energies of the four towers surrounding the cluster's center-of-gravity divided by the cluster energy. A total of five different shower shape variables are used for photon identification and optimized to achieve a high γ^{ID} efficiency of approximately 80% to 90% over the entire E_{T}^{γ} range ($10 < E_{\mathrm{T}}^{\gamma} < 26$ GeV), along with a background rejection rate of approximately 80% at low E_{T}^{γ} and 50% at high E_{T}^{γ}. The requirement is defined as the "tight" γ^{ID} selection.

3.4 Signal Extraction

A photon isolation requirement greatly reduces the contribution of background photons, primarily high-p_{T} neutral mesons decaying to two photons (e.g., $\pi^0 \to \gamma + \gamma$) which form a single cluster. At the reconstruction level, the cluster $E_{\mathrm{T}}^{\mathrm{iso}}$ is calculated by summing the E_{T} of all EMCAL, IHCAL, and OHCAL towers with reconstructed energy above 60 MeV within an isolation cone of radius $\Delta R = 0.3$, excluding the E_{T} of the cluster of interest. An E_{T}^{γ}-dependent $E_{\mathrm{T}}^{\mathrm{iso}}$ threshold is chosen to maintain a 80% isolation efficiency, $E_{\mathrm{T}}^{\mathrm{iso}} < 1.08\ \mathrm{GeV} + 0.03 \times E_{\mathrm{T}}^{\gamma}$.

Even after the "tight" γ^{ID} and isolation requirements, there is still a significant contribution from background photons. This remaining background contribution to the "tight" identified and isolated photons is estimated through a data-driven purity calculation method used in LHC experiments [2, 28]. In this approach, four regions (one signal region and three sideband regions) are defined as follows: A (tight γ^{ID}, isolated), B (tight γ^{ID}, non-isolated), C (non-tight γ^{ID}, isolated), and D (non-tight γ^{ID}, non-isolated) as illustrated in Figure 1. The "non-tight γ^{ID}" is defined as failing any two of the tight shower-shape γ^{ID} requirements, and "non-isolated" is defined as having $E_{\mathrm{T}}^{\mathrm{iso}}$ that exceeds the signal $E_{\mathrm{T}}^{\mathrm{iso}}$ threshold by at least 1 GeV.

The ratio of background yields in region C to region D is assumed to be the same as in region A to region B. To ensure this assumption is valid, the shower shape variables used in the γ^{ID} are optimized to be uncorrelated with $E_{\mathrm{T}}^{\mathrm{iso}}$ for background photons. Assuming that there is no leakage of the signal to region C and D, the number of signal photons in region A is then calculated using:

$$N^{A}_{\mathrm{signal}} = N^{A}_{\mathrm{raw}} - N^{B}_{\mathrm{raw}} \cdot \frac{N^{C}_{\mathrm{raw}}}{N^{D}_{\mathrm{raw}}}, \tag{1}$$

where N^{A}_{signal} is the number of signal photons in region A, and N^{X}_{raw} is the number of photon candidates in region X.

Equation 1 is then modified to account for signal photons leaking into the sideband regions:

$$N^{A}_{\mathrm{signal}} = N^{A}_{\mathrm{raw}} - \left[\left(N^{B}_{\mathrm{raw}} - f^{B,\mathrm{MC}}\, N^{A}_{\mathrm{signal}} \right) \cdot \frac{\left(N^{C}_{\mathrm{raw}} - f^{C,\mathrm{MC}}\, N^{A}_{\mathrm{signal}} \right)}{\left(N^{D}_{\mathrm{raw}} - f^{D,\mathrm{MC}}\, N^{A}_{\mathrm{signal}} \right)} \right] \tag{2}$$

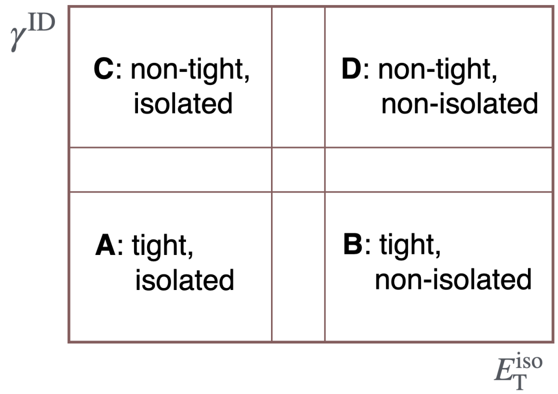

Figure 1: Diagram of the signal region (A) and sideband regions (B, C, D).

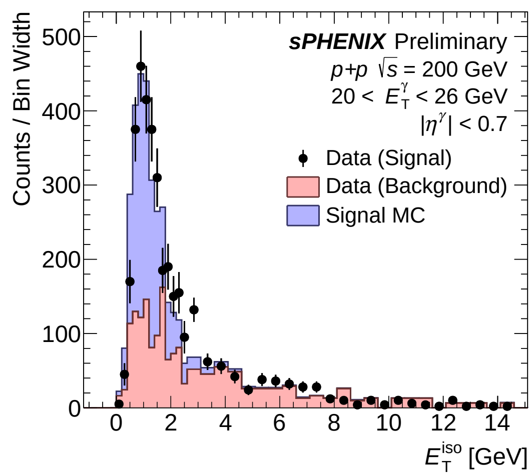

Figure 2: $E_{\mathrm{T}}^{\mathrm{iso}}$ distributions of signal data with tight γ^{ID}, background data with non-tight γ^{ID} and signal MC with tight γ^{ID}. The background data and signal MC histograms are stacked.

where $f^{X,\mathrm{MC}}$ is the ratio of the number of truth-matched signal photons in region X over region A, derived with MC. The purity is defined as the fraction of signal photons relative to the total photon candidates in the signal region A:

$$\mathrm{Purity}(\mathcal{P}) = \frac{N_A^{\mathrm{sig}}}{N_A}. \tag{3}$$

Figure 2 shows the $E_{\mathrm{T}}^{\mathrm{iso}}$ distributions of tight photons (labeled as "Data (signal)") and non-tight photons (labeled as "Data (background)") in data, along with tight photons in MC (labeled as "Signal MC"). The background photon distribution is scaled to match the signal photon distribution in data in the high-$E_{\mathrm{T}}^{\mathrm{iso}}$ region ($E_{\mathrm{T}}^{\mathrm{iso}}$ above 4 GeV). The tight-photon distribution in MC is then added to the scaled non-tight distribution to reproduce the tight-photon distribution in data at small $E_{\mathrm{T}}^{\mathrm{iso}}$. The shape difference in $E_{\mathrm{T}}^{\mathrm{iso}}$ between tight and non-tight γ^{ID} photons is clearly visible.

Figure 3 shows the purity as a function of E_{T}^{γ}. The signal-leakage correction to the purity is at the few-percent level, due to the optimized signal and sideband regions. To smooth out fluctuations,

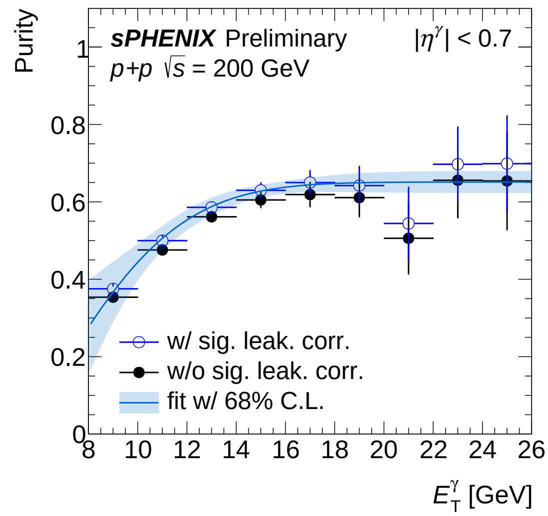

Figure 3: Purity as a function of E_T^γ with and without signal leakage correction in data. The purity with leakage correction is fitted by an error function, the shaded area shows the 68.3% confidence interval of the fit.

the bin-by-bin purity values are fitted with an error function, and the fitted value at each E_T^γ bin center is used to correct the remaining background in "tight"-identified and isolated photons.

3.5 Unfolding

The purity-corrected photon E_T^γ yield distribution is unfolded for E_T^γ using the D'Agostini Bayesian iterative method [29] with the RooUnfold software package version 3.0.5 [30] to account for detector effects such as photon energy resolution. To make the prior of E_T^γ distribution in MC similar to that in data, the response matrix constructed using MC is reweighted using the ratio of purity-corrected yield in data to MC signal photon yield. The number of iterations is set to two, which is chosen to minimize the sum of iteration-dependent changes and statistical uncertainties.

3.6 Efficiency Correction

The trigger, reconstruction, γ^{ID} and isolation efficiencies are estimated by using MC and then applied as corrections to the unfolded E_T^γ spectra. Figure 4 shows the photon reconstruction, γ^{ID} and isolation efficiencies, together with the combined efficiency. All of these efficiencies are applied on a bin-by-bin basis to the spectrum after unfolding.

3.7 Cross-Section Determination

The E_T^γ-differential cross-section of isolated prompt photons is defined as

$$\frac{d^2\sigma}{dE_T^\gamma d\eta} = \frac{1}{\mathscr{L}} \frac{Y^{\mathrm{rec}}}{\mathcal{E}\Delta E_T^\gamma \Delta\eta^\gamma}, \tag{4}$$

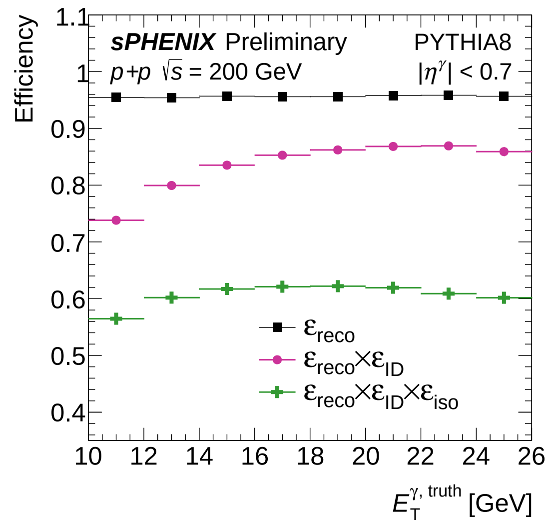

Figure 4: Efficiencies for reconstruction ($\varepsilon_{\rm reco}$), identification ($\varepsilon_{\rm ID}$), isolation requirement ($\varepsilon_{\rm iso}$), and convolved step-by-step efficiencies ($\varepsilon_{\rm tot}$) as a function of truth photon $E_{\rm T}^{\gamma,\,\rm truth}$.

where $\mathcal{E}$ is the combined photon reconstruction, identification, isolation, and MBD trigger efficiency, $\mathscr{L}$ is the integrated luminosity, and $\Delta E_{\rm T}^{\gamma}$ and $\Delta\eta^{\gamma}$ are the bin widths in $E_{\rm T}^{\gamma}$ and η^{γ}, respectively. The integrated luminosity is determined from the minimum-bias trigger cross-section measured in a Vernier scan, and then counting the number of events that satisfy the minimum-bias trigger for the analyzed data. The purity-corrected and unfolded yield, $Y^{\rm rec}$, as a function of $E_{\rm T}^{\gamma}$ is obtained by applying the purity correction and then unfolding, according to

$$Y^{\rm rec}(E_{\rm T}^{\gamma}) \;=\; \text{Unfolded}\left[N^{\rm tight,iso\,\gamma}(E_{\rm T}^{\gamma}) \;\times\; \mathcal{P}(E_{\rm T}^{\gamma})\right], \tag{5}$$

where $N^{\rm tight,iso\,\gamma}$ is the yield of identified and isolated photons and $\mathcal{P}$ is the purity.

4 Systematic Uncertainties

The systematic uncertainties account for the uncertainty on the photon energy scale and resolution, the purity, the unfolding procedure, the efficiency corrections, and the luminosity. Each source of uncertainty is evaluated by repeating the entire analysis with the corresponding variations. In each $E_{\rm T}^{\gamma}$ bin, the relative differences with and without the variations are then added in quadrature to obtain the total uncertainty.

The reconstructed EMCAL tower energy is shifted by 2.6% to account for the photon energy scale uncertainty, based on the differences between data and MC. This is the dominant systematic uncertainty, ranging from 8% to 25% depending on $E_{\rm T}^{\gamma}$.

The systematic uncertainties of the purity are estimated by (1) adjusting the sideband definitions by independently varying the non tight $\gamma^{\rm ID}$ and non isolated criteria, (2) changing the fit function used to extract the purity, and (3) varying the fit result by its 1σ confidence level. Purity is the second largest uncertainty, ranging from 4% to 13%.

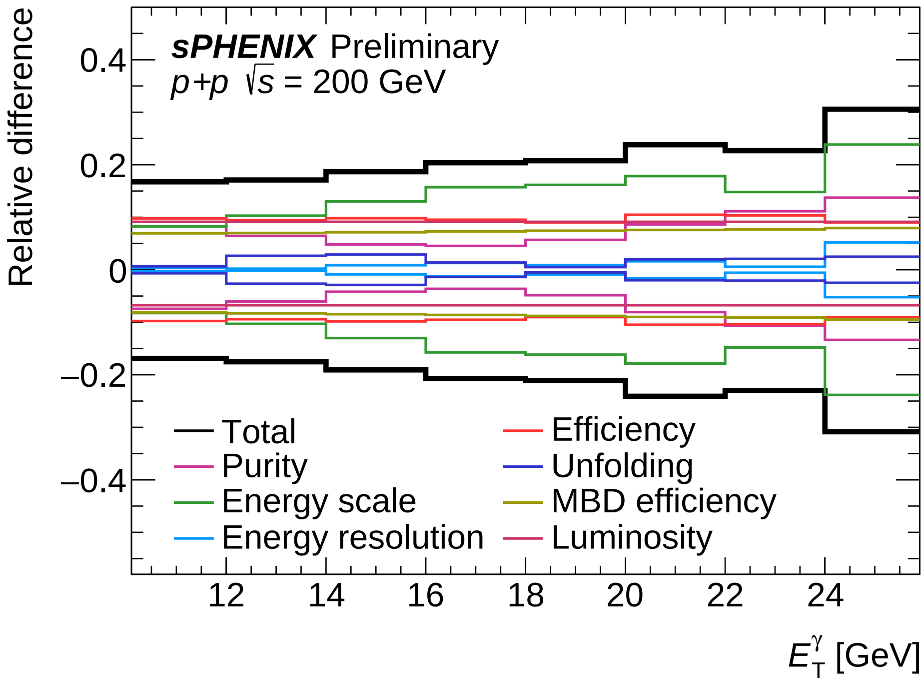

Figure 5: Breakdown of systematic uncertainties as a function of E_{T}^{γ}.

The rest of systematic uncertainties are evaluated as following: First, the efficiency uncertainty is determined by modifying the tight identification criteria and by removing the isolation energy correction in simulation. Second, the unfolding uncertainty is assessed by omitting the reweighting of the MC prior distribution. Third, the photon energy resolution uncertainty is quantified by applying additional smearing to the reconstructed cluster energy in MC simulations. Fourth, the MBD efficiency uncertainty is evaluated by shifting the derived efficiency values upward and downward. Finally, the luminosity uncertainty of $16.6^{+1.4}_{-1.2}$ pb^{-1} is determined by propagating the minimum-bias trigger cross-section measured in the Vernier scan. These contributions are all subdominant compared to other systematic sources. As shown in Figure 5, the total systematic uncertainty ranges from 13% to 30% across the E_{T}^{γ} spectrum and is strongly dependent on E_{T}^{γ}. Since the photon energy scale uncertainty is dominant, the total systematic uncertainty has a strong bin-to-bin correlation.

5 Results

Figure 6 shows the E_{T}^{γ}-differential cross-section. The data are compared with different theoretical predictions. The PYTHIA-8 result uses version 8.307 and the Detroit tune [25]. The JETPHOX v1.3.1_4 calculates cross-sections for both direct and fragmentation photons at NLO. In the JETPHOX calculations, the CT14LO parton distribution functions and the BFG set II [31] fragmentation functions for quarks and gluons into photons are used. The result is also compared with the NLO pQCD calculation provided by W. Vogelsang (following the work in Ref. [15]). For the NLO pQCD calculations, including those from JETPHOX, the renormalization (μ_{R}), factorization (μ_{F}), and

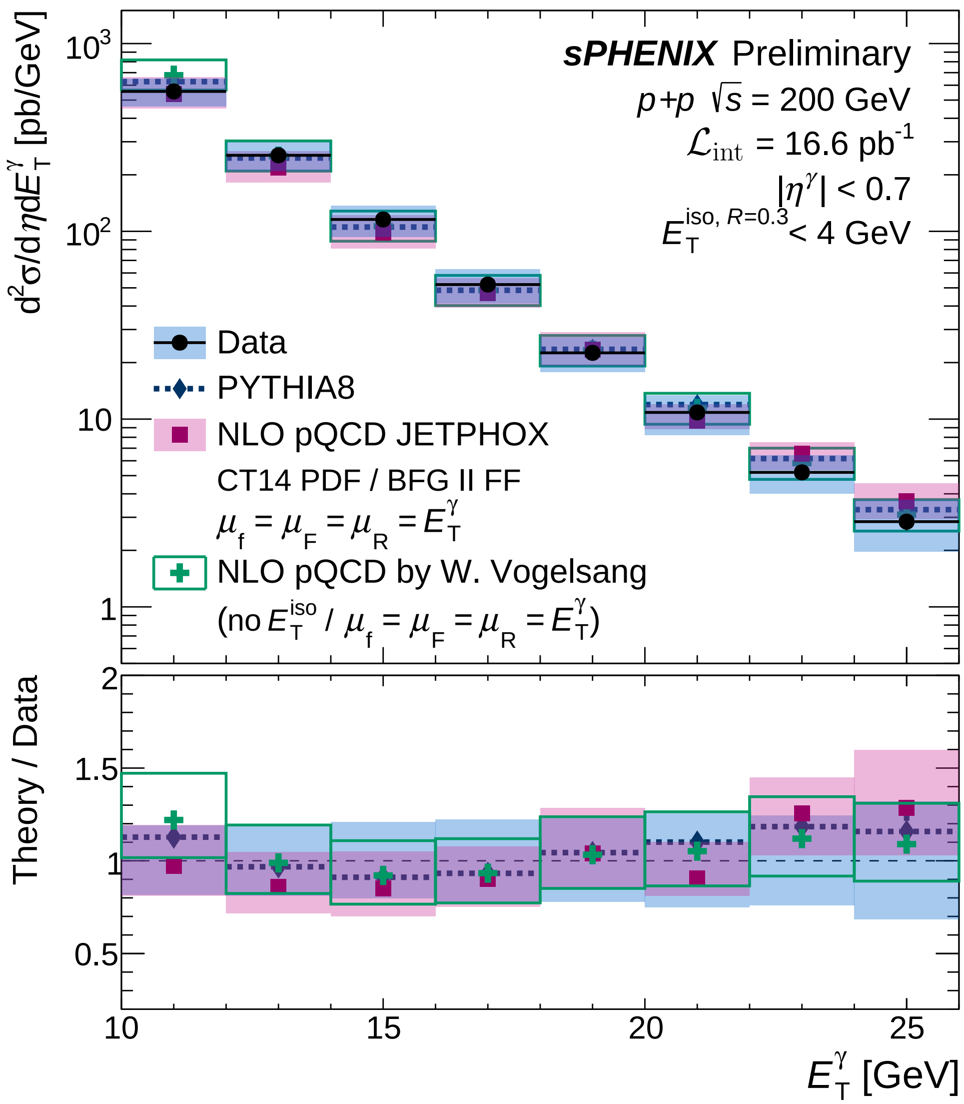

Figure 6: The differential cross-section of isolated prompt photons as a function of E_T^{γ} is compared with theoretical predictions of PYTHIA-8.307 (Detroit tune), JETPHOX and NLO pQCD calculations provided by Werner Vogelsang. The statistical uncertainties are plotted as vertical lines and the systematic uncertainties are plotted as shaded bands. The boxes around the JETPHOX points represent the systematic uncertainties obtained by varying $\mu_f = \mu_F = \mu_R$ to $E_T^{\gamma}/2$ and $2E_T^{\gamma}$. The lower panel shows a theory-to-data ratio for PYTHIA-8, JETPHOX, and NLO pQCD calculations to this analysis, where the experimental systematic uncertainties are shown as shaded bands around unity. The theory and experimental statistical uncertainties are combined on the theory points.

fragmentation (μ_f) scales are all set to E_T^{γ}. The systematic uncertainties are determined by varying these scales to $E_T^{\gamma}/2$ and $2E_T^{\gamma}$. While both PYTHIA-8 and JETPHOX apply the same truth-level isolation criterion used in the data, the calculation by Gordon and Vogelsang does not require a $E_T^{\rm iso}$ condition. All three theoretical predictions are consistent with the data within the quoted uncertainties.

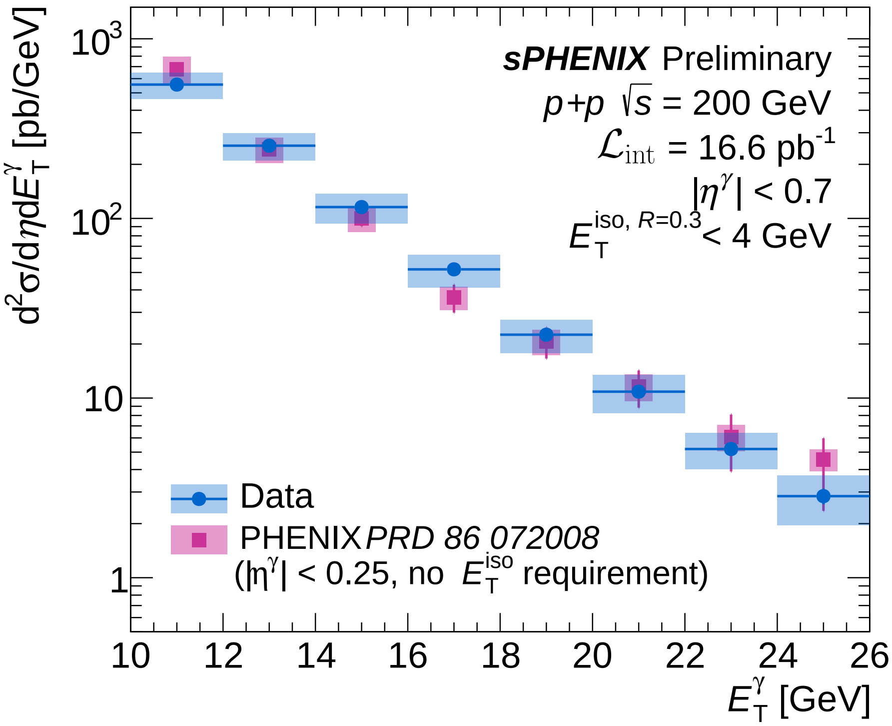

Figure 7: The differential cross-section of isolated prompt photons as a function of E_T^γ is compared with the PHENIX measurements [13] of direct photons. The statistical uncertainties are plotted as vertical lines and the systematic uncertainties are plotted as shaded bands. The PHENIX data points are not corrected for the full E_T^γ bin-width and instead represent the cross-section evaluated at the center of each bin.

The results are also compared with previous measurements reported by the PHENIX experiment [13], as shown in Figure 7. The PHENIX measurement does not require an isolation condition, whereas our results do. Furthermore, the PHENIX data were collected in $|\eta| < 0.25$ and each PHENIX data point represents the cross-section evaluated at the center of its E_T^γ bin rather than being fully integrated over the bin width. Despite these differences, both measurements are consistent within their respective uncertainties.

6 Summary

The differential cross-section of isolated prompt photons is measured in proton–proton collisions at $\sqrt{s} = 200$ GeV using a subset of the data collected during Run 24 with the sPHENIX detector, corresponding to an integrated luminosity of 16.6 pb^{-1}. Photons are measured within $|\eta^{\gamma}| < 0.7$ and $10 < E_{\mathrm{T}}^{\gamma} < 26$ GeV and with an isolation requirement. A data-driven technique is employed for purity estimation, and the measurement is unfolded to account for detector effects. The results are compared with NLO pQCD and MC generator predictions, as well as previous direct-photon measurements reported by the PHENIX experiment [13].

References

[1] CMS Collaboration. Measurement of differential cross sections for inclusive isolated-photon and photon+jets production in proton-proton collisions at $\sqrt{s} = 13$ TeV. *Eur. Phys. J. C*, 79(1):20, 2019. `arXiv:1807.00782`, `doi:10.1140/epjc/s10052-018-6482-9`. 1

[2] ATLAS Collaboration. Measurement of the inclusive isolated prompt photon cross section in pp collisions at $\sqrt{s} = 8$ TeV with the ATLAS detector. *JHEP*, 08:005, 2016. `arXiv:1605.03495`, `doi:10.1007/JHEP08(2016)005`. 1, 3.4

[3] ATLAS Collaboration. Measurement of the inclusive isolated prompt photons cross section in pp collisions at $\sqrt{s} = 7$ TeV with the ATLAS detector using 4.6 fb^{-1}. *Phys. Rev. D*, 89(5):052004, 2014. `arXiv:1311.1440`, `doi:10.1103/PhysRevD.89.052004`. 1

[4] Georges Aad et al. Measurement of the inclusive isolated prompt photon cross-section in pp collisions at $\sqrt{s} = 7$ TeV using 35 pb^{-1} of ATLAS data. *Phys. Lett. B*, 706:150–167, 2011. `arXiv:1108.0253`, `doi:10.1016/j.physletb.2011.11.010`. 1

[5] ALICE Collaboration. Measurement of the inclusive isolated photon production cross section in pp collisions at $\sqrt{s} = 7$ TeV. *Eur. Phys. J. C*, 79(11):896, 2019. `arXiv:1906.01371`, `doi:10.1140/epjc/s10052-019-7389-9`. 1

[6] ALICE Collaboration. Measurement of the inclusive isolated-photon production cross section in pp collisions at $\sqrt{s} = \mathbf{13}$ TeV. *Eur. Phys. J. C*, 85(1):98, 2025. `arXiv:2407.01165`, `doi:10.1140/epjc/s10052-024-13506-x`. 1

[7] ALICE Collaboration. Measurement of isolated prompt photon production in pp and p-Pb collisions at the LHC. 2 2025. `arXiv:2502.18054`. 1

[8] ATLAS Collaboration. Measurement of prompt photon production in $\sqrt{s_{\mathrm{NN}}} = 8.16$ TeV p+Pb collisions with ATLAS. *Phys. Lett. B*, 796:230–252, 2019. `arXiv:1903.02209`, `doi:10.1016/j.physletb.2019.07.031`. 1

[9] CMS Collaboration. The production of isolated photons in PbPb and pp collisions at $\sqrt{s_{\mathrm{NN}}} = 5.02$ TeV. *JHEP*, 07:116, 2020. `arXiv:2003.12797`, `doi:10.1007/JHEP07(2020)116`. 1

[10] ALICE Collaboration. Measurement of the inclusive isolated-photon production cross section in pp and Pb$-$Pb collisions at $\sqrt{s_{\mathrm{NN}}} = 5.02$ TeV. 9 2024. `arXiv:2409.12641`. 1

[11] ATLAS Collaboration. Centrality, rapidity and transverse momentum dependence of isolated prompt photon production in lead-lead collisions at $\sqrt{s_{\mathrm{NN}}} = 2.76$ TeV measured with the ATLAS detector. *Phys. Rev. C*, 93(3):034914, 2016. `arXiv:1506.08552`, `doi:10.1103/PhysRevC.93.034914`. 1

[12] M. Harrison, T. Ludlam, and S. Ozaki. RHIC project overview. *Nucl. Instrum. Meth. A*, 499(2):235–244, 2003. doi:10.1016/S0168-9002(02)01937-X. 1

[13] PHENIX Collaboration. Direct-Photon Production in $p+p$ Collisions at $\sqrt{s} = 200$ GeV at Midrapidity. *Phys. Rev. D*, 86:072008, 2012. arXiv:1205.5533, doi:10.1103/PhysRevD.86.072008. 1, 7, 5, 6

[14] Patrick Aurenche, Michel Fontannaz, Jean-Philippe Guillet, Eric Pilon, and Monique Werlen. A New critical study of photon production in hadronic collisions. *Phys. Rev. D*, 73:094007, 2006. arXiv:hep-ph/0602133, doi:10.1103/PhysRevD.73.094007. 1

[15] L. E. Gordon and W. Vogelsang. Polarized and unpolarized prompt photon production beyond the leading order. *Phys. Rev. D*, 48:3136–3159, 1993. doi:10.1103/PhysRevD.48.3136. 1, 5

[16] Torbjörn Sjöstrand, Stefan Ask, Jesper R. Christiansen, Richard Corke, Nishita Desai, Philip Ilten, Stephen Mrenna, Stefan Prestel, Christine O. Rasmussen, and Peter Z. Skands. An introduction to PYTHIA 8.2. *Comput. Phys. Commun.*, 191:159–177, 2015. arXiv:1410.3012, doi:10.1016/j.cpc.2015.01.024. 1, 3.2

[17] A. Adare et al. An Upgrade Proposal from the PHENIX Collaboration. 2015. arXiv:1501.06197. 2

[18] Ron Belmont et al. Predictions for the sPHENIX physics program. *Nucl. Phys. A*, 1043:122821, 2024. doi:10.1016/j.nuclphysa.2024.122821. 2

[19] The sPHENIX Collaboration. sPHENIX Technical Design Report, PD-2/3 Release, 2019. URL: https://indico.bnl.gov/event/7081/attachments/25527/38284/sphenixtdr20190513.pdf. 2

[20] Henry Klest. Overview and design of the sPHENIX TPC. *J. Phys. Conf. Ser.*, 1498:012025, 2020. arXiv:2110.02082, doi:10.1088/1742-6596/1498/1/012025. 2

[21] S. Aune et al. The sPHENIX Micromegas Outer Tracker. *Nucl. Instrum. Meth. A*, 1066:169615, 2024. doi:10.1016/j.nima.2024.169615. 2

[22] C. A. Aidala et al. Design and Beam Test Results for the 2-D Projective sPHENIX Electromagnetic Calorimeter Prototype. *IEEE Trans. Nucl. Sci.*, 68(2):173–181, 2021. doi:10.1109/TNS.2020.3034643. 2

[23] C. A. Aidala et al. Design and Beam Test Results for the sPHENIX Electromagnetic and Hadronic Calorimeter Prototypes. *IEEE Trans. Nucl. Sci.*, 65(12):2901–2919, 2018. doi:10.1109/TNS.2018.2879047. 2

[24] T. G. O'Connor et al. Design and testing of the 1.5 T superconducting solenoid for the BaBar detector at PEP-II in SLAC. *IEEE Trans. Appl. Supercond.*, 9:847–851, 1999. doi:10.1109/77.783429. 2

[25] Manny Rosales Aguilar, Zilong Chang, Raghav Kunnawalkam Elayavalli, Renee Fatemi, Yang He, Yuanjing Ji, Dmitry Kalinkin, Matthew Kelsey, Isaac Mooney, and Veronica Verkest. pythia8 underlying event tune for RHIC energies. *Phys. Rev. D*, 105(1):016011, 2022. arXiv:2110.09447, doi:10.1103/PhysRevD.105.016011. 3.2, 5

[26] S. Agostinelli et al. Geant4—a simulation toolkit. *Nuclear Instruments and Methods in Physics Research Section A: Accelerators, Spectrometers, Detectors and Associated Equipment*, 506(3):250–303, 2003. doi:10.1016/S0168-9002(03)01368-8. 3.2

[27] G. David, E. Kistenev, S. White, C. Woody, A. Bazilevsky, S. Belikov, V. Kochetkov, V. Onuchin, and A. Usachev. Pattern recognition in the PHENIX PbSc electromagnetic calorimeter. *IEEE Trans. Nucl. Sci.*, 47:1982–1986, 2000. doi:10.1109/23.903833. 3.3

[28] ATLAS Collaboration. Measurement of the cross section for inclusive isolated-photon production in pp collisions at $\sqrt{s} = 13$ TeV using the ATLAS detector. *Phys. Lett. B*, 770:473–493, 2017. arXiv:1701.06882, doi:10.1016/j.physletb.2017.04.072. 3.4

[29] G. D'Agostini. Improved iterative Bayesian unfolding. In *Alliance Workshop on Unfolding and Data Correction*, 10 2010. arXiv:1010.0632. 3.5

[30] Tim Adye. Unfolding algorithms and tests using RooUnfold. In *PHYSTAT 2011*, pages 313–318, Geneva, 2011. CERN. arXiv:1105.1160, doi:10.5170/CERN-2011-006.313. 3.5

[31] L. Bourhis, M. Fontannaz, and J. P. Guillet. Quark and gluon fragmentation functions into photons. *Eur. Phys. J.*, 2(3):529–537, 1998. arXiv:hep-ph/9704447, doi:10.1007/s100529800708. 5